Title

Temporal subtraction contrast-enhanced dedicated breast CT

Journal

Physics in Medicine and Biology, 61(17)

ISSN

0031-9155

Authors

Gazi, Peymon M

Aminololama-Shakeri, Shadi

Yang, Kai

et al.

Publication Date

2016-09-07

DOI

10.1088/0031-9155/61/17/6322

Peer reviewed

HHS Public Access

Author manuscript

Phys Med Biol. Author manuscript; available in PMC 2017 September 07.

Published in final edited form as:

Phys Med Biol. 2016 September 7; 61(17): 6322–6346. doi:10.1088/0031-9155/61/17/6322.

Temporal subtraction contrast-enhanced dedicated breast CT

Peymon M. Gazi[1,2], **Shadi Aminololama-Shakeri**[2], **Kai Yang**[3], and **John M. Boone**[1,2,a)]

[1]Department of Biomedical Engineering, University of California, Davis, One Shields Avenue, Davis, California, 95616

[2]Department of Radiology, University of California, Davis Medical Center, 4860 Y street, Suite 3100 Ellison Building, Sacramento, California 95817

[3]Department of Radiology, Massachusetts General Hospital, 55 Fruit Street Boston, MA 2114

Abstract

Purpose—To develop a framework of deformable image registration and segmentation for the purpose of temporal subtraction contrast-enhanced breast CT is described.

Methods—An iterative histogram-based two-means clustering method was used for the segmentation. Dedicated breast CT images were segmented into background (air), adipose, fibroglandular and skin components. Fibroglandular tissue was classified as either normal or contrast-enhanced then divided into tiers for the purpose of categorizing degrees of contrast enhancement. A variant of the Demons deformable registration algorithm, Intensity Difference Adaptive Demons (IDAD), was developed to correct for the large deformation forces that stemmed from contrast enhancement. In this application, the accuracy of the proposed method was evaluated in both mathematically-simulated and physically-acquired phantom images. Clinical usage and accuracy of the temporal subtraction framework was demonstrated using contrast-enhanced breast CT datasets from five patients. Registration performance was quantified using Normalized Cross Correlation (NCC), Symmetric Uncertainty Coefficient (SUC), Normalized Mutual Information (NMI), Mean Square Error (MSE) and Target Registration Error (TRE).

Results—The proposed method outperformed conventional affine and other Demons variations in contrast enhanced breast CT image registration. In simulation studies, IDAD exhibited improvement in MSE(0–16%), NCC (0–6%), NMI (0–13%) and TRE (0–34%) compared to the conventional Demons approaches, depending on the size and intensity of the enhancing lesion. As lesion size and contrast enhancement levels increased, so did the improvement. The drop in the correlation between the pre- and post-contrast images for the largest enhancement levels in phantom studies is less than 1.2% (150 Hounsfield units). Registration error, measured by TRE, shows only submillimeter mismatches between the concordant anatomical target points in all patient studies. The algorithm was implemented using a parallel processing architecture resulting in rapid execution time for the iterative segmentation and intensity-adaptive registration techniques.

Conclusion—Characterization of contrast-enhanced lesions is improved using temporal subtraction contrast-enhanced dedicated breast CT. Adaptation of Demons registration forces as a

a) john.boone@ucdmc.ucdavis.edu.

function of contrast-enhancement levels provided a means to accurately align breast tissue in pre- and post-contrast image acquisitions, improving subtraction results. Spatial subtraction of the aligned images yields useful diagnostic information with respect to enhanced lesion morphology and uptake.

Keywords

Breast cancer imaging; Cone beam CT; Deformable image registration; Image segmentation

I. INTRODUCTION

The use of contrast agents in breast imaging has been shown to substantially increase breast cancer detection, and contrast uptake has been shown to correlate with benign/malignant status[1]. Dynamic Contrast Enhanced (DCE) breast MRI is considered the standard of care for patients at high risk for developing breast cancer and has been shown to improve sensitivity with some reduction in specificity[2–4]. The use of iodinated contrast agent in dedicated breast CT has also been shown to have diagnostic potential[1]. Recently a number of investigators have studied contrast-enhanced digital mammography and contrast-enhanced tomosynthesis using dual-energy subtraction methods[5–7].

Digital subtraction angiography is a vascular imaging procedure in which planar projection images of the patient are acquired before and after the injection of iodinated contrast agent. These planar images are subtracted, pixel by pixel, to eliminate contrast of the normal tissue parenchyma and thus demonstrate the vascular anatomy. Although contrast agent injection is used frequently with whole body computed tomography (CT), temporal subtraction methods have generally not been utilized. Energy subtraction is used in whole body CT however, with and without contrast agent injection, in order to differentiate soft tissue, bone and calcified plaque from vascular and parenchymal contrast agent. In general, the use of contrast agent combined with the 3-D imaging capabilities of whole body CT is powerful enough that temporal subtraction methods are not necessary.

In breast cancer screening and diagnostic breast imaging, the specific morphology of a lesion and its contrast uptake characteristics are important diagnostic clues[8–10]. To better quantify spatial patterns of contrast uptake in breast CT, temporal subtraction methods may help to better demonstrate a lesion on 3-D breast CT image data sets. In this study, temporal subtraction of pre-and post-contrast injection breast CT data sets was investigated. Unlike digital subtraction angiography, where image acquisition has high temporal resolution (sub-second) to address rapid arterial blood flow kinetics, the acquisition of volumetric breast CT requires on the order of 10–16 seconds per data set. Furthermore, from a (brachial access) venous injection, contrast agent perfusion of the breast takes place over time frames from 20 – 200 seconds. This longer time period between pre-contrast and post-contrast imaging can and does result in patient movement between acquisitions, which in turn results in spatial deformations between the two 3-D volume data sets to be subtracted. Because of this it is generally necessary to perform image registration between the pre-contrast and post-contrast breast CT data sets. Rigid registration methods can be used to register gross movements of the breast between image acquisitions. While the high malleability of breast tissue often

results in non-linear, non-rigid movement in the breast upon patient motion, non-rigid (deformable) registration methods are required to correct for breast motion before temporal subtraction between the 3-D volume data sets can be routinely performed.

In this investigation, a previously reported deformable registration algorithm (Demons[11]) was substantially modified to address the needs of this application. Different versions of this algorithm have been proposed, and a range of applications have reported benefits from use of this technique[12–18]. Deformable registration techniques are typically performed between two data sets with equivalent intensity scaling. However, the post-contrast breast CT volume data set usually contains considerable enhancement around the lesion of interest and elsewhere. This significantly changes the gray scale levels between the pre- and post-contrast images, which reduces the effectiveness of standard Demons approaches. In order to compensate for this discontinuity between the data sets, regions of contrast enhancement are identified using segmentation techniques on the non-subtracted contrast-enhanced data set prior to the application of deformable image registration methods. With the proposed algorithm, this segmented region is used with a modified energy function to optimize the registration process.

II. METHODS AND MATERIALS

Successful temporal subtraction of breast CT images requires accurate deformable image registration prior to subtraction. During the deformable registration, displacement forces are calculated using tiered segmented images. Different tissue types are identified using a custom two-means clustering image segmentation method. The accuracy of the framework is evaluated through simulation, phantom and patient studies. A summary of notation associated with the methods, images and validation techniques is provided in Table 1.

A. Image segmentation framework

A three dimensional segmentation method based on the smoothed two-means clustering algorithm[19, 20] was proposed to segment bCT images. The algorithm generates a segmented image with floating point format that specifies the tissue type corresponding to that of the original image. Assigned voxel values are as follows: air (0.0), adipose (1.0), fibro-glandular (2.1 – 2.9, depending upon glandularity), contrast enhanced (3.1 – 3.9, depending on the degree of contrast enhancement) and skin (5.0). Value 4.0 is reserved for the further algorithm development in the future. As shown in Figure 1, the following steps are taken to implement two-means clustering segmentation.

Stage 1. Given the number of bins (N), a histogram, $H(n)$, based on the bCT image is generated. The maximum and minimum Hounsfield Units (HU)[21] in the image are found. As a convention, the number of bins is determined by the whole numbers between HU_{max} and HU_{min}. HU_{max} and HU_{min} are also used to find the low-bound (n_{LB}), high-bound (n_{HB}) and mid-bound (n_{MB}) bin values.

Stage 2. Each two-means histogram based clustering routine begins by taking $H(n)$, n_{LB}, n_{MB} and n_{HB} as input arguments. The lower-interval and higher-interval average values (AV_{LI} and AV_{HI}) are calculated using the input

arguments and are then compared to check convergence. Convergence is achieved if the difference between AV_{HI} and AV_{LI} is less than a parameter, ε. High values of ε result in rapid convergence, lower values converge more slowly. In our application ε was set to 0.01. During each iteration n_{LB}, n_{MB} and n_{HB} values are updated. The bin value at convergence (T_1) specifies the threshold between breast tissue and background.

Stage 3. n_{LB} is set to T_1. Histogram-based two means clustering is implemented to find a new value for n_{LB}. This value is set to the threshold between adipose and other breast tissue (T_2).

Stage 4. Ratio of T_1 and T_2, T_1/T_2, is calculated and compared to the value found in the previous iteration. A three dimensional median filter with a kernel size of three cubic voxels is applied to smooth the image (unless convergence has been reached) at which point the two-means clustering algorithm ends. The minimal 3-D median filter is defined as a seven-point kernel in order to avoid over-smoothing that would obscure the fine details of the bCT image. The smoothed image generated from the last iteration is utilized in subsequent stages. Upon convergence, T_A is found by scanning the histogram from the left edge toward the right edge until a bin is reached with the lowest frequency that is at least 1% of the total histogram height.

Shown in Figure 2, the following steps are used to segment contrast-enhanced voxels.

Stage 5. The peak and valley pattern of the two-means clustering method's smoothed image histogram is analyzed to generate segmentation. For smoothing, a ten element wide RECT function is convolved with the histogram. The logarithm of the smoothed histogram is used to enhance local minima and maxima. Two-means clustering results in the separation of fibroglandular from adipose components of the histogram (Figure 2.b).

Stage 6. A difference calculation between the pre- and post-contrast histograms results in a contrast-agent defining histogram (Figure 2.c) through which P_C and T_C are found.

Stage 7. An overlay of Figure 2.b and Figure 2.c along with the application of a color gradient provides a visualization of the segmentation values (Figure 2.d). The fibroglandular segmentation values are separated into ten equally-spaced tiers between T_{FG} and T_C bins and then between T_C and $(P_C + (P_C - T_C))$. These tiers allow for glandularity and contrast enhancement level classification, respectively. Any voxel in I_s containing an intensity larger than $(P_C + (P_C - T_C))$ and not marked as skin, belongs to the highest contrast-enhancement tier.

Stage 8. Voxels in the post-contrast segmented image, $S(n)$, are assigned values based on corresponding voxels in $H(n)$ by the following:

$$S(n)=\begin{cases} 0.0, & n<T_A,\ air \\ 1.0, & T_A \le n<T_{FG},\ adipose \\ 2.x, & T_{FG} \le n<T_C,\ glandular \\ 3.y, & T_C \le n,\ contrast \\ 4.0, & reserved \\ 5.0, & skin \end{cases} \quad (1)$$

where x and y are integers between 0 and 9.

Stage 9. In order to delineate the skin from other breast tissues, coronal slices are analyzed starting from vertical and horizontal image borders and moving inwards. Once the shift from background to tissue is recognized, a line profile with a thickness of 3 mm is generated[22]. The line profile's peak, representing the midpoint of the skin, provides a value by which the inner border of the skin is defined. The actual skin thickness is the minimum of the calculated vertical and horizontal thicknesses. Pixels corresponding to skin are assigned a value of 5.0 in the segmented image.

B. Image registration framework

A complete contrast-enhanced breast CT procedure results in the generation of two fully tomographic breast CT image sets. The breast is scanned before and after contrast material injection. Due to the heterogeneous and elastic nature of breast tissue, repositioning of the patient on the bCT system during the contrast material administration leads to local non-linear deformations[23]. Rigid registration methods are not well suited for aligning pre-contrast and post-contrast images. In designing a deformable registration framework for contrast-enhanced breast CT, the following considerations were addressed:

1. Sub-millimeter accuracy is required when employing any deformable registration technique in breast CT.
2. Voxel intensity conservation assumption (i.e. the assumption of minimal image intensity change between equivalent anatomical points on the pre- and post-con images) cannot be made.
3. Margin boundaries should be preserved in diagnostically challenging lesions types, such as foci (small lesions) and non-mass-like enhanced lesions.
4. Execution time of the registration algorithm should be realistic for clinical work flow.

The Demons image registration algorithm[24] is a common procedure for fast greyscale image-based registration. A generalized method of Demons deformation field[17] is calculated using

$$\overrightarrow{D(p)} = (M(p) - F(p)) \frac{\overrightarrow{(\nabla I(p))}}{\left\|\overrightarrow{\nabla I(p)}\right\|^2 + \frac{\sigma^2}{k^2}} \quad (2)$$

where D is the estimated displacement, p is a given voxel in the moving (pre-contrast) image, M and F are the moving (pre-contrast) and fixed (post-contrast) images and k is the normalization factor accounting for spatial uncertainty on the Demons correspondences. The arrows emphasize that each element of the deformation field or gradient matrix is a three element vector specifying the orientation in orthogonal coordinates. The variable k is set to the mean-squared value of the image voxel size[25]. The variable σ is the image intensity noise set to $[M(p) - F(p)]$. Variable I can be set to M or F to generate passive[11] or active force[14] vectors calculated based on the gradient (represented by) of moving or fixed images, respectively. The gradient of the post-contrast image ($\overrightarrow{\nabla F(p)}$) is highly dependent upon the contrast uptake in any given voxel (p). The intensity conservation assumption of the basic hypothesis of the Demons algorithm is violated due to the contrast changes produced by contrast enhancement in CE-bCT. Large contrast enhancement leads to large deformation vectors and correspondingly large registration errors.

Combining the passive and active forces symmetrically leads to rapid convergence[14, 18, 26]. Revisiting (2) by combining both active and passive force deformation vectors and accounting for contrast enhancement in the post-contrast image yields IDAD (Intensity Difference Adaptive Demons):

$$\overrightarrow{D(p)} = (M(p) - F(p)) \left(\frac{\overrightarrow{(\nabla F(p).c(p) + \nabla M(p))}}{\left\|\overrightarrow{\nabla F(p).c(p) + \nabla M(p)}\right\|^2 + \frac{[M(p) - F(p)]^2}{k^2}} \right). \quad (3)$$

In IDAD, $c(p)$ has been defined as the Intensity Difference Correction Factor (IDCF), a variable introduced to the symmetric Demons to change the active force amplitude based on the enhancement tier assigned to p as described in Sec. II.A. IDCF is used to normalize the post-contrast image gradient considering that the internal force originating from the difference in voxel intensity of neighboring points within the post-contrast image originates solely from the contrast material. Introducing IDCF in (3) does not change the well-posed criterion without which the deformation field becomes unstable[13]. IDCF is defined at every voxel as

$$c(p) = \frac{2 \times P_C - T_C - F(p)}{2 \times (P_C - T_C)}. \quad (4)$$

In (4), $2 \times (P_C - T_C)$ acts as a normalizing factor: if $F(p)$ is equal to T_C (the low bound of the contrast-enhanced region in the contrast enhancement histogram shown in Figure 2.d), IDCF is 1. If $F(p)$ is equal to $2 \times P_C - T_C$ (the high bound of the contrast-enhanced region), IDCF is

0. As a result, the active Demons forces are normalized linearly according to the intensity difference between pre-contrast and post-contrast image voxels. IDCF is set to one for voxels not marked as contrast-enhanced in the corresponding segmented image and is set to zero for voxels marked as contrast-enhanced in the corresponding segmented image that have intensities greater than $2\times P_C - T_C$. The parameters used in IDAD framework are determined automatically and independent of user interaction.

Figure 3 is a graphical representation of the deformation forces defined in actual patient bCT images calculated using IDAD and the conventional variations of Demons. The images shown in Figure 3.a and b were acquired from a patient scan. Figure 3.a shows a coronal slice of the pre-contrast image and Figure 3.b shows the corresponding coronal slice in the post-contrast image. The pre-contrast image was first aligned to the post-contrast image using affine registration, then registered using multi-level Demons[25, 27]. The deformation field arising from Demons is comprised of a matrix. The matrix size corresponds to that of the pre-contrast image. Each voxel within the matrix is a vector. Each vector represents the displacement of the corresponding voxel in the pre-contrast image along orthogonal Cartesian axes. The norm of each vector is the displacement step length. Figure 3 represents the norms of the deformation field. The deformation norm images have been gray-scale coded to represent the displacement length (Figure 3.d–g). Successful alignment of the pre and post-contrast images generates a subtracted image that is utilized for clinical analysis. Improper registration results in artificial deformation of lesion boundaries within the subtracted image. The magnified regions shown in Figure 3.h–k, reveal the impact that intensity variations have upon the strength of Demons forces.

Taking the gradient of an image results in large vector norms around contrast enhanced lesions. These vectors generate forces that artificially deform the boundaries of the enhanced lesion in the subtracted image (I_{sub}). When contrast boundaries are present within the lesion, such as the necrotic interior tissue, misregistration of inner boundaries may occur. Due to the fact that contrast enhancement is not uniform within the enhanced lesions[28], lesion structure may be significantly deformed if the forces are not normalized. The modified forces alleviate these deformations as shown in Figure 3.g.

The proposed registration technique is comprised of the following steps: Segmentation; performed on M and F following the technique outlined in Sec. II.A. and an affine 3D registration based on regular step gradient descent optimization of mean square errors, which is performed primarily to account for breast translational, rotational or shearing displacement that may have occurred between the pre- and post-contrast scans. The UC Davis architecture of dedicated breast CT is comprised of a cone-beam CT system installed upon a gantry that performs one full rotation around the breast. The patient is positioned pendantly on the scanner table-top. A contrast-enhanced bCT study is comprised of a pre-contrast scan followed by a post-contrast scan. Patients are positioned on the scanner before and after contrast injection with the breast at the center of rotation. As a result, the scaling factor of the affine matrix is small, though the translational or shearing factors may not be. The affine registration matches the overall positioning of the breast volume in pre- and post-contrast images but does not account for complex changes in anatomical structure of the breast tissue. Multi-resolution Demons, a well-known pyramid architecture used to improve

robustness while avoiding extra iterations in the Demons framework (caused by local minima and maxima)[29], is used to down-sample the pre- and post-contrast images by successive factors of 8, 4, 2 and 1. At each of these down-sampled levels, forces are calculated using IDAD. The deformation fields obtained from IDAD calculations at each pyramid level are used to initialize the calculation at the subsequent level. After the iterations have been completed within a level, the difference between the newly generated deformation field and the deformation field found in the previous step is calculated by voxel-wise vector subtraction. When a magnitude of at least 99% of the difference vectors is smaller than one-tenth the voxel size, IDAD is considered convergent[15]. The sum of the calculated deformations results in the overall IDAD deformation field.

C. Validation studies

The proposed hybridized method of CE-bCT image segmentation/registration was evaluated quantitatively in three ways:

1. Simulation study: Mathematical deformations were applied on an actual patient pre-contrast bCT image set. A contrast-enhanced lesion was simulated and placed within the deformed images.
2. Phantom study: A custom deformable physical breast phantom, with a deformable phantom lesion that could be placed into the breast phantom, was fabricated and imaged on the bCT system used for patient scans with manual deformation produced between acquisitions.
3. Patient study: Five CE-bCT patient data sets exhibiting a range of deformation and structural complexities were selected and processed through the IDAD sequence.

C.1. Mathematical phantom study—Deformations were simulated using previously-acquired patient bCT images. Due to the elasticity of breast tissue, it may undergo significant deformation during bCT imaging. An image data set can be transformed to produce deformation; however, if done so arbitrarily, the resulting deformation may not represent clinical reality. Therefore, a realistic mathematical forward-deformation matrix was generated using patient CE-bCT scans to allow for quantitative validation of the proposed IDAD method.

The 3D image dataset was selected based on shape, glandular distribution, deformations in the anatomical structure, intensity and size of the contrast enhancement. The size of the breast in the selected bCT dataset is near the population average with a diameter of 14.4 cm and a length 1.5 times the radius[22]. The patient in the selected dataset was repositioned on the scanner between pre- and post-contrast scans resulting in considerable deformation of the observed breast anatomy. Repositioning of the patient resulted in imaging some anatomy in the post-contrast image (the ribs, for example) that is not seen in the pre-contrast image.

To synthesize a post-contrast image, the patient's pre-contrast breast CT image was mathematically deformed using a known deformation field. A mathematically generated

enhanced lesion was placed within the deformed image, effectively synthesizing a post-contrast image. Figure 4 illustrates the method described in the following:

a. The pre-contrast image was registered to the post-contrast image using affine transform. A coronal slice of the transformed image is shown in Figure 4.a.

b. The registered pre-contrast image is then aligned with the post-contrast image using homologous pairs of landmarks (fiducials). A thin plate spline (TPS)[30] method was used to deform the post-affine, pre-contrast image based on the fiducials placed within it. For each fiducial, the corresponding anatomical landmark in the post-contrast image was manually found and then used to warp the image via TPS. Inclusion of the entire breast volume in generating a deformation field was critical; the accuracy of the registration, however, was not. The three-dimensional image was divided vertically into nine equal 1 cm sections along the transverse direction from chest wall to nipple. In each image section, nine fiducials – four skin and five glandular- were placed across the tissue (Figure 4.a). Skin fiducials were positioned on each extreme of the anterior, posterior, left and right lateral parts of the skin. The glandular fiducials were positioned on the glandular tissue at each mid-point between the skin fiducials. A ninth marker was placed centrally within the glandular tissue, nearest the breast dorsal-ventral axis. The corresponding position of each fiducial marker was manually found in the post-contrast image (Figure 4.b). In order to cover the entire slab volume, each fiducial was placed 1 mm apart from the preceding fiducial in the axial direction. The last marker was placed on the nipple. Within the generated deformation field, each vector voxel corresponding to the voxel outside of the breast volume was set to zero. Due to the repositioning of the patient on the scanner between the pre- and post-contrast scans, a large displacement of the fiducials was observed. The resulting deformed image resembles a large deformation that may occur within a breast image between pre- and post-contrast scans. Figure 4.c shows the color-coded deformation field projected on the corresponding slice of the post-affine, pre-contrast image. Each voxel in the deformation field is a vector representing the movement of the voxel in the coronal, sagittal or transverse directions, and the norm of each vector was color-mapped in Figure 4.c for visualization purposes.

c. Contrast-enhancement was introduced into the deformed image. In this study, a synthetic lesion was generated using a normally distributed symmetric morphology. The surface profile of the generated homogenous oval enhancement type is shown in Figure 4.e. A three dimensional Gaussian distribution with intensity peaks of 50, 100 and 150 HU, and enhancement diameters of 15, 20 and 25 mm were defined. The synthetic lesion was inserted within a region of glandular tissue in the warped pre-con image. The contrast agent placement extends to both adipose and

fibro-glandular tissue, increasing the attenuation coefficient of the whole region (Figure 4.f). Therefore, the simulated contrast enhancement not only occurs primarily within the glandular tissue, but also extends to the adipose tissue.

d. The deformation field resulting from fiducial-based TPS represents the "template" deformation field (ground truth). The deformation field resulting from IDAD is compared to the template deformation field using Mean Square Error (MSE)[31], Normalized Cross Correlation (NCC)[32] and Normalized Mutual Information (NMI)[33] metrics. In calculating MSE, the absolute values of the vectors in the deformation fields are used. IDAD results were compared against those of passive, active and symmetric force Demons. In addition, the registration accuracy was measured by finding the Target Registration Error (TRE)[25] between the pre-contrast image and the synthesized post-contrast image. Since the deformation field is known, the error between a voxel in the pre-contrast image and the mapped position of the same voxel in the synthesized post-contrast image is also known and is defined as the absolute value of the mapping vector. The average value of all the errors is TRE. This metric is used to compare the performance of all the Demons variations.

C.2. Physical phantom study—A phantom study was performed in order to validate the robustness of the proposed method. An anthropomorphic breast phantom, produced using an actual patient breast CT data set image was previously fabricated using a computer controlled water-jet cutting technique[34] as displayed in Figure 5. Thermoplastic, representing skin, was formed into a container. Polyethylene was used to represent adipose tissue. The breast volume was cut along the anterior/posterior axis to generate 62 slices, each 1.59 mm thick. The segmented glandular tissue was cut out of each slice using computer-controlled water jet cutting. The flexibility of coronal slice positioning was ± 1–3 mm and ±1–5 degrees in rotation around the A/P axis. Two liquid compounds, representative of normal and contrast-enhanced fibroglandular tissues based on their x-ray attenuation properties were made and inserted into the glandular cavities as explained below:

A. **Pre-contrast phantom construction:** A 1.3% molarity alginic acid (a natural polymer obtained from kelp and seaweed) solution was formed to represent fibroglandular tissue. The density of the "glandular solution" corresponds to that of water, a surrogate normally used for fibroglandular tissue[35]. The thermoplastic skin forms a container which was filled with adipose-density equivalent vegetable oil (Wasso Energy, Waterbury, CT). Each polyethylene slab was then inserted into the phantom. Compression was applied during insertion to reduce air bubble formation. The fibroglandular solution was then poured into the phantom glandular cavities until full. These steps resulted in a pre-contrast breast phantom. This phantom was scanned on the same breast CT prototype used for patient scans reported in this paper. A total number of 500 projection views were acquired at 80 kV and 9 mA with an additional 0.3 mm Cu

filtration. These data were used to reconstruct a 512×512×512 matrix, representing the 3D image data of the phantom.

B. **Post-contrast phantom construction:** Following the pre-contrast scan, the phantom was deconstructed by removing the slices from the phantom breast volume. Step A was then repeated, generating a deformed version of the pre-contrast phantom. In order to generate deformable contrast enhanced lesions, a 2.6% molarity calcium carbonate solution was made. To this solution, four different volumes of an iodine contrast agent (Visipaque 270; GE Healthcare, Waukesha, WI) were added to obtain three concentrations of iodinated solution: 1.62, 3.24 and 4.86 mg/ml. These three iodine solutions were used to simulate different contrast agent uptake levels in breast tissue. The contrast material was injected into the glandular solution with a flexible tipped syringe. Upon interaction with alginic acid solution, the iodine solution forms a membrane around the contrast material which generates a deformable volume and prevents the contrast solution from dissolving into the glandular solution. These steps resulted in a manually deformed breast phantom with a contrast-enhanced "lesion" inserted. This phantom was scanned with the same technique factors as before. Different volumes of iodine solutions - 0.6, 1.2 and 1.8 ml - were used to simulate the lesion in the post-contrast phantom. Care was taken while performing the injections in order to avoid further deformation. After each injection, the phantom was scanned. A total of five scans were performed for each concentration of iodine solution.

The reconstructed pre-contrast image was registered to the deformed pre-contrast and post-contrast phantom images using the framework outlined in Sec. II.B.

The hypothesis of the phantom study was that the IDAD algorithm results in similar registration performance despite changes in the amount of contrast enhancement. Demons forces are derived from the absolute value and derivative of intensity differences within and between the fixed and moving images (Equation 2). In order to assess the performance of the IDAD algorithm as a function of contrast enhancement, an entropy based similarity metric, Symmetric Uncertainty Coefficient (SUC)[27, 36], was used. SUC is defined as

$$SUC_X = \frac{2M\,(X, I_{pre-con})}{E(X) + E\,(I_{pre-con})} \quad (5)$$

where M and E denote the mutual information and marginal entropy operators applied on the images. X may be either the deformed pre-contrast image or the post-contrast image. SUC incorporates the entropies of the individual normalized image intensity histograms in the form of Mutual Information (MI) and is increased with structural similarity between the images[36, 37]. In order to define a base-line for the comparison purposes of SUC values derived from each iodine concentration phantom scan, the normalized SUC is defined as

$$SUC_N = \frac{SUC_{Post-contrast} - SUC_{deformed\ pre-contrast}}{SUC_{deformed\ pre-contrast}} \quad (6)$$

By focusing on only the acquired deformed images in the numerator and denominator, this normalization enables a comparison between the effect of different concentrations of iodine on mutual information between post-contrast images acquired at different concentrations and the corresponding pre-contrast images. Assuming for each concentration of iodinated contrast agent that the structure of the phantom is unchanged, SUC_N values should have minimal variance.

In order to ensure that the materials used in the phantom construction were a reasonable replica of the contrast-enhanced breast tissues, a quantitative evaluation was performed. A custom fabricated 15 cm diameter uniform polyethylene phantom was used for testing. Five inserts filled with vegetable oil (surrogate for adipose tissue), 1.33 molar alginic acid solution (surrogate for fibroglandular tissue) and 1.6, 3.2 and 4.8 mg/ml iodine solutions (surrogate for contrast enhanced tissue) were placed into the phantom and scanned using equivalent technique values as those employed with the physical deformable phantom.

C.3. Patient study—Data sets from five patient scans, obtained during a study of lesion conspicuity[1], were selected in order to evaluate the performance of IDAD on real patient scans. Approval of the institutional review board and the Radiation Use Committee and written informed consent were obtained for this HIPAA-compliant study. The five selected cases have different breast density, breast size, lesion size, contrast uptake and deformation attributes. The IDAD algorithm was applied to these five cases. The accuracy of IDAD was measured by comparing the registered pre-contrast and the post-contrast images using MSE, NCC and Target Registration Error (TRE - a physical measure of accuracy)[38, 39] to evaluate the image registration pipeline's performance.

The level of difficulty of the image registration task varies among the selected patient datasets. Anatomical target points were selected and registration accuracy was measured across the targets to generate TRE. Six targets were used in all cases and were manually positioned in the image dataset as follows: a target was positioned on the anterior aspect of the pectorals muscle, a second target on the nipple and one on each extreme of the anterior, posterior, medial and lateral borders of the fibroglandular tissue on the mid-coronal slice of the CT image. Within each case, additional targets were placed based on breast anatomy characteristics.

i. Case 1. An irregular mass with indistinct borders was identified within a dense breast with a mild degree of enhancement (50 HU on average) and deformations. The definitive surgical pathology finding was ductal carcinoma in-situ (DCIS). Two additional targets were positioned in the center of the lesion and on the biopsy marker clip.

ii. Case 2. An irregular mass, 11.5 mm in diameter, with spiculated margins was identified within a large volume breast with scattered fibroglandular

tissue. The mass demonstrated avid contrast enhancement (110 HU in average). Minor movement occurred between acquisition of the pre-and post-contrast datasets. Biopsy of the mass demonstrated invasive mammary carcinoma (IMC). Two additional targets were positioned on each extreme of the anterior and posterior edges of the contrast-enhanced lesion.

iii. Case 3. An area of non-mass enhancement 5 mm in diameter with an average of 60 HU was identified in a dense breast with moderate background parenchymal enhancement. Biopsy of this lesion showed DCIS. Two additional targets were positioned on the center and anterior corner of the enhanced lesion.

iv. Case 4. Significant movement occurred between pre- and post-contrast scans with this patient. An oval enhancing mass with an average contrast enhancement of 70 HU was identified in a breast with scattered fibroglandular tissue. Core biopsy demonstrated invasive ductal carcinoma (IDC). Two additional target points were positioned on the center and posterior corner of the enhanced lesion.

v. Case 5. An extremely dense breast of small volume was repositioned on the scanner between the pre and post-contrast scans, resulting in large deformations. A small round enhancing mass measuring 85 HU on average was present. Lung tissue and ribs are observed in both pre- and post-contrast images, causing irregular maxima in the image histograms which affect the amplitude of the Demons forces. An additional target point was placed on the most posterior location of the observed ribs. A final additional target point was placed on the medial corner of the enhanced lesion.

C.4. Validation metrics—The primary thrust of this study was to demonstrate the adaptive nature of IDAD in dealing with contrast enhancement. A number of metrics were used to evaluate the performance of IDAD against other variations of Demons. When there is either similarity or a linear relationship between the intensity of voxels in moving and fixed images, intensity-based registration metrics such as MSE and NCC have been used. In those patients where the contrast enhancement is minimal, this class of metrics is a viable validation tool. Entropy-based registration metrics such as NMI and SUC are standard when registering images acquired using different modalities. In CE-bCT patient scans, where the voxel values of corresponding anatomical locations in pre- and post-contrast images may differ by a measure of up to 150 HU1, the usage of these types of metrics in CE-bCT is appropriate as pre- and post-contrast images may differ to an extent similar to that of images generated by different modalities (voxel values are different, and anatomical fixtures exist in the pre- or post-contrast that do not exist in the other). Though a laborious, manual registration metric, TRE is considered to be “exact” and of particular value in patient studies due to the direct radiologist participation. The limited number of targets in TRE however, cause it to suffer from quantum variations. Mathematical simulation, in which the template deformation is known, minimizes these variations. TRE, therefore, can be calculated for all

voxels of the fixed and moving images (in a 512×512×512 reconstruction for example) within each variation of Demons.

D. Computational performance

Custom software was developed for the hybridized image segmentation/registration method proposed in this paper. The software was written in C++ (Visual Studio 2010, MicroSoft Corporation, Seattle, WA) and was run on a quad-core system with 32 GB memory (Alienware Corporation, Miami, FL) and a Graphical Processor Unit (GeForce GTX 690 GPU, NVIDIA Co., Santa Clara, CA). The smoothing filter portion of the image segmentation outlined in Sec. II.A was implemented in GPU, while the CPU-based multi-threading was used to implement the two-means thresholding procedure shown in Figure 1. For a typical 512 × 512 × 512 dataset, 2 seconds were required for each iteration of the segmentation algorithm. For all the patient cases reported in this paper, segmentation converged in less than 12 iterations. The IDAD registration code was written for GPU when calculating the deformations at downsampled levels of 8, 4 and 2 (DS8, DS4 and DS2). The GPU used for this application did not have enough memory to contain the DS1 level registration. Therefore, the code for DS1 was written separately for CPU operation. The GPU code was written in OpenCL (Khronos Group, Beaverton, OR). The framework outlined in open source Insight Toolkit (ITK, Kitware Inc., Clifton Park, NY) was adopted to incorporate affine and IDAD into the in-house software application[40]. The average registration time for a typical 512 × 512 × 512 CT dataset (patient cases 2, 3 and 4) was 126 seconds. Image registration was carried out prior to the radiologist's viewing session.

III. RESULTS

A. Mathematical phantom study

The mathematical contrast enhancement added to the deformed simulated image results in different performances between the registration techniques as explained in Sec. II.B. In Figure 6, IDAD is compared with the conventional versions of the Demons algorithm. The degradation in registration accuracy represented by MSE and NCC stems from the intensity variations between the pre-contrast and the synthesized post-contrast images. In the cases with small lesions (10 mm in diameter), the degradation is negligible (Figure 6.a and d). For these cases, the MSE and NCC computed over the entire image volume are comparable for symmetric Demons and IDAD. Performance difference is more readily observed at higher enhancement levels (Figure 6.c). For large enhancement levels (25 mm in diameter), without adaptive correction of active demon forces, MSE and NCC rapidly degrade with increased voxel intensity (Figure 6.c and f). The amount of degradation depends on the specific variant of the Demons algorithm. This stems from the influence of the active forces in measuring force amplitude. The contribution of the active force increases in techniques where the uncorrected active forces are employed, such as symmetric Demons.

Figure 7 demonstrates an absolute comparison between registration techniques. In small lesions with small contrast enhancement levels, IDAD performs relatively similarly to symmetric Demons (the relative difference between the two methods is 2%). This is due to the weak corrections (IDCF close to 1) associated with the enhanced voxels. At large

enhancement levels however, IDAD limits the active forces, thereby preventing artificial degradations that result from intensity differences.

The greatest improvement is observed when the largest and highest level of contrast enhancement is simulated and positioned within the deformed pre-contrast image (Figure 7). Comparing IDAD with other variations of Demons, improvements in validation metrics are 0–16% in MSE, 0–6% in NCC, 0–13% in NMI and 0–12% in TRE.

B. Physical phantom study

Table 2 shows the results of scanning the HU calibration phantom, fabricated as explained in II.C.2. Similar to the mathematical phantom study, the contrast-enhanced tissue surrogates fall into classes of 60 HU enhancement levels per 1.62 mg/ml iodinated solution. This confirms the use of the employed materials.

Figure 8 illustrates the convergence behavior of IDAD in phantom data and provides an initial evaluation of registration accuracy in CBCT imaging of breast. This figure shows the evolution of IDAD convergence between subsample levels. In order to make a comparison between different volumes and concentrations of iodine possible, a constant number of iterations (30), was used in each subsample level. The progression of convergence is evident at all concentrations. At each concentration level, the mutual information between the pre- and post-contrast images increases, thereby reducing the SUC_N. A similar trend in convergence is observed in all lesion volumes.

Figure 9 shows the difference in SUC_N between the deformed pre-contrast phantom and the contrast-enhanced phantom in each volume category. Each bar represents the concentration class's average deviation value when convergence is reached. As shown, SUC_N values for small volumes of injected contrast material, regardless of different concentrations of iodine, fall below 0.1 percent. At larger volumes of contrast material, the impact on SUC_N is greater. Nonetheless, the maximum error, occurring at the largest volume (1.8 ml) and highest concentration of iodine (4.8 mg/ml), remains under 1.2%.

C. Patient scan study

Figure 10 shows the validation of the IDAD algorithm for all five patient cases in this study. Rows demonstrate different stages of the registration pipeline as outlined in Sec. II.A and B. Coronal, sagittal, axial and magnified coronal views of the contrast-enhanced lesion are shown. In all cases the first and second rows demonstrate the pre- and post-contrast images, with the same window and level settings. The third row shows the segmented image derived from the post-contrast image. The fourth row shows the results of the subtraction of the post-contrast image using only rigid registration (affine) between pre and post-contrast image datasets. In the last row, the results of IDAD - with window-level settings identical to that of the fourth row images - are shown.

As shown in Table 3, the IDAD algorithm results in superior alignment of the pre-contrast to post-contrast images based upon all metrics. NCC between all post-IDAD registered, pre-contrast images and the corresponding post-contrast images is above 0.99. The structural similarities between the images involved in registration, represented by NMI, increases.

MSE, a direct measure of image pixel value similarity, drops. Registration error measured by TRE shows submillimeter mismatches between the concordant anatomical target points in all but one case (case 5). Affine registration shows improvement over unregistered images in more difficult registration tasks (cases 3–5), but produces errors in several areas of the breast. Spanning over different deformations, employing IDAD in CE-bCT registration produces excellent accuracy in registering the pre- to the post-contrast images, producing three dimensional temporal-subtraction contrast-enhanced bCT which can be used as a tool in not only measuring size and morphology of the contrast-enhanced lesion, but also in quantifying the level of contrast enhancement. The enhancement levels indicated in Table 3 summarize the average value of the enhanced lesion in the subtracted images. A visual comparison between the magnified image of the lesion in the subtracted image (row 5) and the magnified image of the same segmented slice (row 3) highlight IDAD's effectiveness in correctly registering the enhanced voxels.

IV. DISCUSSION AND CONCLUSIONS

Previous studies have shown that for non-calcified lesions detected by mammography, mass shape and margin are important predictors of malignancy[10]. Specifically, irregular shape and spiculated margins as defined by the BI-RADS lexicon[41] on mammography have been shown to have the highest positive predictive values for cancer[10]. Micro-calcifications are routinely described by their morphology and distribution on mammography. The BI-RADS descriptors with highest malignant association for micro-calcifications are linear morphology and linear or segmental distribution[10]. With modalities utilizing contrast material such as breast MRI, masses are characterized by their size, shape, margin and internal enhancement and areas of non-mass enhancement (NME) by their distribution and enhancement patterns. Irregular shape, spiculated margins and heterogeneous internal enhancement characteristics have the highest positive predictive values for malignancy in mass lesions[8, 9]. Clumped NME in a ductal distribution has been shown to be a predictor for malignancy in non-mass lesions on MRI[9]. In early studies with dedicated contrast enhanced breast CT, malignant masses enhanced significantly more than benign masses which offered a potential quantitative method for predicting malignancy. Preliminary data have shown that malignant calcifications due to ductal carcinoma in-situ enhance significantly more than benign micro-calcifications[1]. Hence, an accurate assessment of lesion size, shape, margin and enhancement pattern on dedicated breast CT is essential for lesion characterization and prediction of malignancy. Accurate determination of the size and extent of lesion enhancement is important for pre-operative staging of malignant lesions - one of the accepted indications for performing contrast based imaging of breast tumors.

The Demons algorithm is commonly used in deformable registration tasks for its accuracy, speed and simplicity. In both its original and variant forms, however, it produces registration errors that render it unsuitable for contrast-enhanced breast CT. Conventional Demons variations result in distortions both within and around enhanced lesions and the severity increases with the enhancement level. Assuming that quantification of contrast enhancement provides valuable diagnostic information[1], it is important to correct for the large displacement vectors that artificially deform the shape of the enhanced lesion in the subtracted image.

We have studied the impact of varying demon forces over different volumes and contrast enhancement levels. We find that registration accuracy is lowest for active force Demons when used in cases with large breast volumes and high levels of contrast enhancement. The simulation study shows that the symmetric forces Demons, containing an uncorrected fixed image gradient, as the active force Demons does, is also less than optimal due to the perturbing influence of added contrast agent. Therefore, an automatic correction of the fixed image gradients was investigated. As a first step, segmentation of different tissue types using two-means clustering was incorporated into the image registration framework. Segmentation classifies the contrast-enhancement into different tiers. The voxels belonging to different contrast-enhancement levels are treated differently in deriving the deformation vector. The iodine segmentation results are an intrinsic component of the new form of Demons. Proposed here, this hybridized framework of image segmentation and registration is called IDAD. Simulation results demonstrate the performance improvement using IDAD over other variations of Demons.

In the case of the simulations designed to evaluate the performance of the IDAD algorithm, the deformation field is known. Changing the volume size and enhancement level of the contrast-enhanced lesion results in new deformations which are compared to the known field. As discussed in Sec. II.C.1, IDAD demonstrates better registration accuracy compared to conventional Demons variations, specifically in cases of large enhancement within large volumes of tissue. The phantom study was implemented in order to apply IDAD to datasets acquired in clinical environments. A previously described deformable phantom was used to study the progression of IDAD through the multiscale pyramid. Results show a drop in the mutual information to the order of less than 1.2% from the template deformations, suggesting that applying IDAD results in minor mismatches with the reference deformation.

The patient cases, selected for their varying characteristics, provide a clinical quantitative assessment of IDAD compared to the original unregistered and affine registered cases. In all cases IDAD showed greater accuracy in registration of pre-contrast to post-contrast images compared to affine registration. The contrast enhancement in the 3-dimentional subtracted images follows the same pattern as shown in segmented images, proving the consistency of the method in correctly registering the concordant pre-contrast and contrast-enhanced tissue in pre- and post-contrast images.

In-house standalone software was developed for incorporating different aspects of IDAD, providing radiologists and researchers with tools necessary to analyze the properly registered images. The ability to register images quickly and accurately in a manner that is robust against contrast-enhancement variations was the primary goal of developing the IDAD framework. The ability to register images quickly and accurately in a manner that is robust against contrast-enhancement variations was the primary goal of developing the IDAD framework.

Computed tomography of the breast is a true 3-D imaging modality, and therefore delivers coherent views in three orthogonal views as well as off axis multi-planar views. It has been reported that contrast-enhanced breast CT can be potentially used in predicting the malignancy of a mass. Moreover, correctly identifying the contrast-enhanced lesion’s size

and enhancement levels using temporal subtraction can further assist radiologists in achieving high levels of diagnostic accuracy. Ongoing work in our laboratory includes qualitative analysis of the CE-bCT image data and comparing the results with those derived from IDAD.

Acknowledgments

This work was supported in part by two research grants (Grant No. 7EB-0075 and 11I-0114) from California Breast Cancer Research Program, a research grant (R01 CA89260) from National Cancer Institute, and a research grant (R01 EB002138) from the National Institute of Biomedical Imaging and Bioengineering. The authors would like to express thanks to Dr. Karen Lindfors for her feedback and guidance, and Dr. Andrea Ferrero for his assistance with evaluation techniques.

References

1. Prionas ND, Lindfors KK, Ray S, Huang SY, Beckett LA, Monsky WL, Boone JM. Contrast-enhanced Dedicated Breast CT: Initial Clinical Experience. Radiology. 2010; 256:714–723. [PubMed: 20720067]
2. Kuhl CK, Schild HH, Morakkabati N. Dynamic bilateral contrast-enhanced MR imaging of the breast: trade-off between spatial and temporal resolution. Radiology. 2005; 236:789–800. [PubMed: 16118161]
3. Padhani AR, Khan AA. Diffusion-weighted (DW) and dynamic contrast-enhanced (DCE) magnetic resonance imaging (MRI) for monitoring anticancer therapy. Targeted oncology. 2010; 5:39–52. [PubMed: 20383784]
4. Kuhl CK, Schrading S, Bieling HB, Wardelmann E, Leutner CC, Koenig R, Kuhn W, Schild HH. MRI for diagnosis of pure ductal carcinoma in situ: a prospective observational study. Lancet. 2007; 370:485–492. [PubMed: 17693177]
5. Diekmann F, Diekmann S, Jeunehomme F, Muller S, Hamm B, Bick U. Digital mammography using iodine-based contrast media: initial clinical experience with dynamic contrast medium enhancement. Investigative radiology. 2005; 40:397–404. [PubMed: 15973130]
6. Dromain C, Thibault F, Muller S, Rimareix F, Delaloge S, Tardivon A, Balleyguier C. Dual-energy contrast-enhanced digital mammography: initial clinical results. European radiology. 2011; 21:565–574. [PubMed: 20839001]
7. Jong RA, Yaffe MJ, Skarpathiotakis M, Shumak RS, Danjoux NM, Gunesekara A, Plewes DB. Contrast-enhanced digital mammography: initial clinical experience. Radiology. 2003; 228:842–850. [PubMed: 12881585]
8. Gutierrez RL, DeMartini WB, Eby PR, Kurland BF, Peacock S, Lehman CD. BI-RADS lesion characteristics predict likelihood of malignancy in breast MRI for masses but not for nonmasslike enhancement. AJR American journal of roentgenology. 2009; 193:994–1000. [PubMed: 19770321]
9. Mahoney MC, Gatsonis C, Hanna L, DeMartini WB, Lehman C. Positive predictive value of BI-RADS MR imaging. Radiology. 2012; 264:51–58. [PubMed: 22589320]
10. Liberman L, Abramson AF, Squires FB, Glassman JR, Morris EA, Dershaw DD. The breast imaging reporting and data system: positive predictive value of mammographic features and final assessment categories. AJR American journal of roentgenology. 1998; 171:35–40. [PubMed: 9648759]
11. Thirion, JP. presented at the Computer Vision and Pattern Recognition, 1996. Proceedings CVPR ‘96, 1996 IEEE Computer Society Conference on; 1996. (unpublished)
12. Cahill ND, Noble JA, Hawkes DJ. A Demons algorithm for image registration with locally adaptive regularization. Medical image computing and computer-assisted intervention : MICCAI … International Conference on Medical Image Computing and Computer-Assisted Intervention. 2009; 12:574–581.
13. Vercauteren T, Pennec X, Perchant A, Ayache N. Non-parametric diffeomorphic image registration with the demons algorithm. Medical image computing and computer-assisted intervention :

MICCAI … International Conference on Medical Image Computing and Computer-Assisted Intervention. 2007; 10:319–326.

14. Wang H, Dong L, O'Daniel J, Mohan R, Garden AS, Ang KK, Kuban DA, Bonnen M, Chang JY, Cheung R. Validation of an accelerated 'demons' algorithm for deformable image registration in radiation therapy. Physics in medicine and biology. 2005; 50:2887–2905. [PubMed: 15930609]
15. Nithiananthan S, Brock KK, Daly MJ, Chan H, Irish JC, Siewerdsen JH. Demons deformable registration for CBCT-guided procedures in the head and neck: convergence and accuracy. Medical physics. 2009; 36:4755–4764. [PubMed: 19928106]
16. Nithiananthan S, Schafer S, Mirota DJ, Stayman JW, Zbijewski W, Reh DD, Gallia GL, Siewerdsen JH. Extra-dimensional Demons: A method for incorporating missing tissue in deformable image registration. Medical physics. 2012; 39:5718–5731. [PubMed: 22957637]
17. Vercauteren T, Pennec X, Perchant A, Ayache N. Diffeomorphic demons: Efficient non-parametric image registration. NeuroImage. 2009; 45:S61–S72. [PubMed: 19041946]
18. Zhou L, Zhou L, Zhang S, Zhen X, Yu H, Zhang G, Wang R. Validation of an improved 'diffeomorphic demons' algorithm for deformable image registration in image-guided radiation therapy. Bio-medical materials and engineering. 2014; 24:373–382. [PubMed: 24211919]
19. Nelson TR, Cerviño LI, Boone JM, Lindfors KK. Classification of breast computed tomography data. Medical physics. 2008; 35:1078–1086. [PubMed: 18404942]
20. Packard, N.; Boone, JM. presented at the SPIE 6510, Medical Imaging 2007: Physics of Medical Imaging, 651038; 2007. (unpublished)
21. Yang, K. PhD thesis. University of California; Davis: 2007. Development and Evaluation of a Dedicated Breast CT Scanner.
22. Huang SY, Boone JM, Yang K, Packard NJ, McKenney SE, Prionas ND, Lindfors KK, Yaffe MJ. The characterization of breast anatomical metrics using dedicated breast CT. Medical physics. 2011; 38:2180–2191. [PubMed: 21626952]
23. Guo Y, Sivaramakrishna R, Lu CC, Suri J, Laxminarayan S. Breast image registration techniques: a survey. Med Bio Eng Comput. 2006; 44:15–26. [PubMed: 16929917]
24. Thirion JP. Image matching as a diffusion process: an analogy with Maxwell's demons. Medical Image Analysis. 1998; 2:243–260. [PubMed: 9873902]
25. Nithiananthan S, Schafer S, Uneri A, Mirota DJ, Stayman JW, Zbijewski W, Brock KK, Daly MJ, Chan H, Irish JC, Siewerdsen JH. Demons deformable registration of CT and cone-beam CT using an iterative intensity matching approach. Medical physics. 2011; 38:1785–1798. [PubMed: 21626913]
26. Yang D, Goddu SM, Lu W, Pechenaya OL, Wu Y, Deasy JO, El Naqa I, Low DA. Technical note: deformable image registration on partially matched images for radiotherapy applications. Medical physics. 2010; 37:141–145. [PubMed: 20175475]
27. Santos J, Chaudhari AJ, Joshi AA, Ferrero A, Yang K, Boone JM, Badawi RD. Non-rigid registration of serial dedicated breast CT, longitudinal dedicated breast CT and PET/CT images using the diffeomorphic demons method. Physica medica : PM : an international journal devoted to the applications of physics to medicine and biology : official journal of the Italian Association of Biomedical Physics (AIFB). 2014; 30:713–717.
28. Yang K, Kwan ALC, Huang SY, Packard NJ, Boone JM. Noise power properties of a cone-beam CT system for breast cancer detection. Medical physics. 2008; 35:5317–5327. [PubMed: 19175091]
29. Kostelec PJ, Weaver JB, Healy DM Jr. Multiresolution elastic image registration. Medical physics. 1998; 25:1593–1604. [PubMed: 9775363]
30. Wenhong, S.; Weidong, Z.; Mingqiang, Y. presented at the Bioinformatics and Biomedical Engineering, (iCBBE) 2011 5th International Conference on; 2011. (unpublished)
31. Anandan P. A computational framework and an algorithm for the measurement of visual motion. Int J Comput Vision. 1989; 2:283–310.
32. Sarvaiya, JN.; Patnaik, S.; Bombaywala, S. presented at the Advances in Computing, Control, & Telecommunication Technologies, 2009. ACT '09. International Conference on; 2009. (unpublished)

33. Opposits G, Kis SA, Tron L, Berenyi E, Takacs E, Dobai JG, Bognar L, Szucs B, Emri M. Population based ranking of frameless CT-MRI registration methods. Zeitschrift fur medizinische Physik. 2015
34. Prionas ND, Beckett LA, McKenney SE, Chen L, Stern RL, Boone JM. Monte Carlo study of the effects of system geometry and antiscatter grids on cone-beam CT scatter distributions. Medical physics. 2013; 40:051915. [PubMed: 23635285]
35. Prionas ND, Huang SY, Boone JM. Experimentally determined spectral optimization for dedicated breast computed tomography. Medical physics. 2011; 38:646–655. [PubMed: 21452702]
36. Melbourne, A.; Hawkes, D.; Atkinson, D. presented at the Biomedical Imaging: From Nano to Macro, 2009. ISBI '09. IEEE International Symposium on; 2009. (unpublished)
37. Wong KK, Yang ES, Wu EX, Tse HF, Wong ST. First-pass myocardial perfusion image registration by maximization of normalized mutual information. Journal of magnetic resonance imaging : JMRI. 2008; 27:529–537. [PubMed: 18183575]
38. Fitzpatrick JM, West JB. The distribution of target registration error in rigid-body point-based registration. IEEE transactions on medical imaging. 2001; 20:917–927. [PubMed: 11585208]
39. Castillo R, Castillo E, Guerra R, Johnson VE, McPhail T, Garg AK, Guerrero T. A framework for evaluation of deformable image registration spatial accuracy using large landmark point sets. Physics in medicine and biology. 2009; 54:1849–1870. [PubMed: 19265208]
40. Gazi, P. PhD thesis. University of California; Davis: 2015. Advancement of Spatial Resolution in Dedicated Breast CT.
41. D'Orsi, C.; Sickles, EA.; Mendelson, EB.; Morris, EA., et al. ACR BI-RADS Atlas, Breast Imaging Reporting and Data System. American College of Radiology; Reston, VA: 2013.

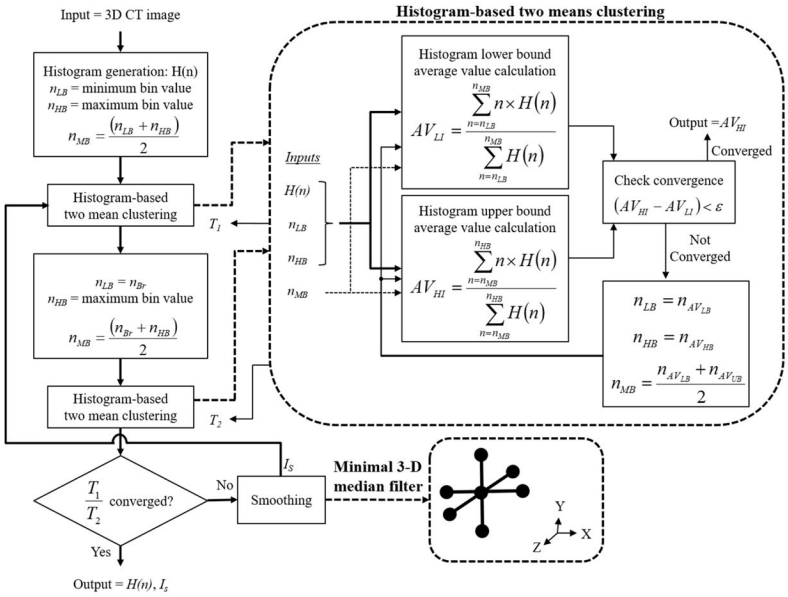

Figure 1.
Breast two-means clustering segmentation scheme

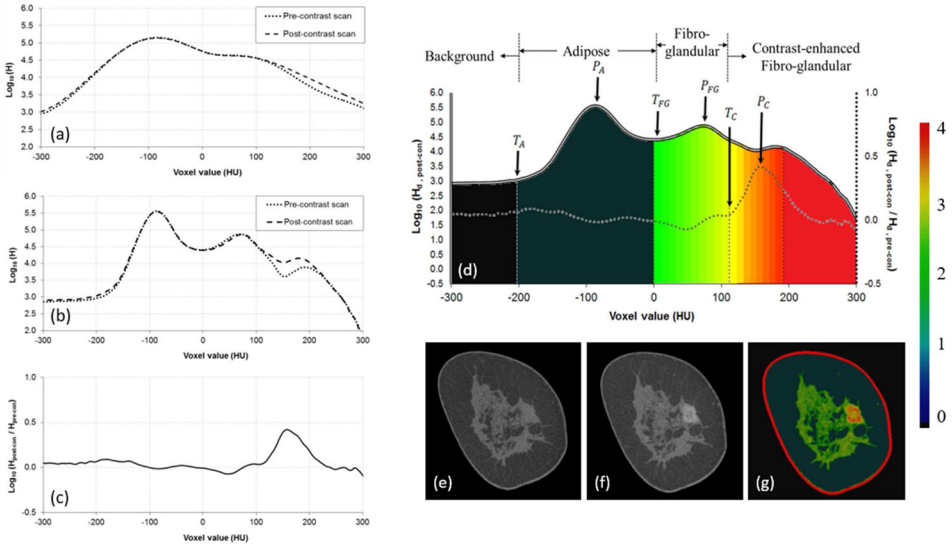

Figure 2.

bCT Histogram-based Segmentation. (a) Histogram of pre-contrast and post-contrast images before two-means clustering, (b) Histogram of pre-contrast and post-contrast images after two-means clustering, (c) Subtraction of the pre- and post-contrast curves shown in (b), (d) Overlay of the post-contrast image after two-means clustering on the contrast curve shown in (c), (e) A coronal slice of pre-contrast image, (f) Corresponding coronal slice in post-contrast image, (g) Corresponding segmented coronal slice.

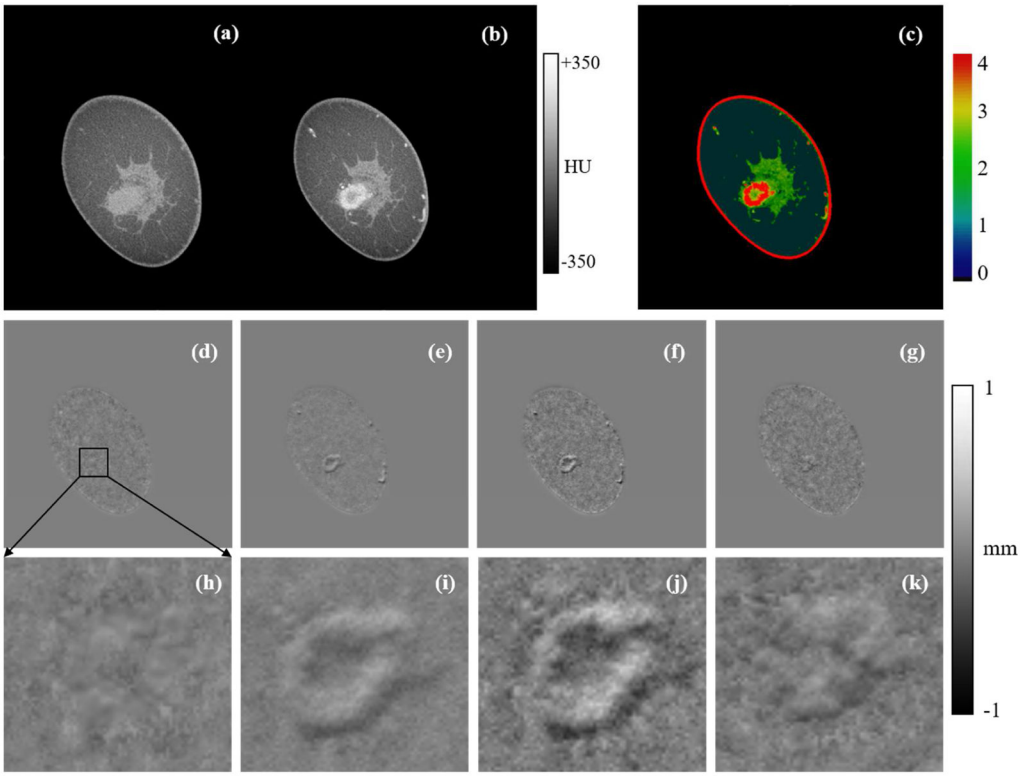

Figure 3.

Deformations resulting from conventional Demons forces and IDAD. (a) Pre-contrast image registered to post-contrast image shown in (b) using an affine transform along with the post-contrast segmented image shown in (c). Deformation step lengths resulting from passive, active, symmetric and IDAD are shown in (d), (e), (f) and (g) respectively. The insets demonstrated in (h)–(k) show magnified views of the deformations shown in (d)–(g) around the contrast-enhanced lesion.

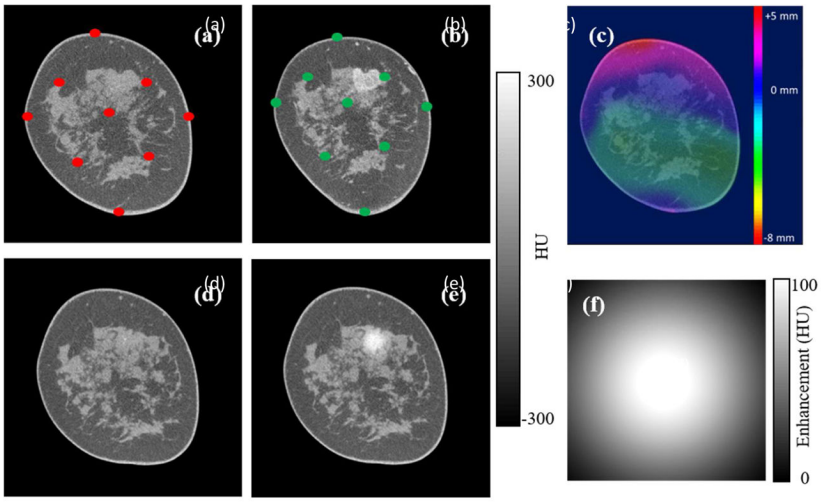

Figure 4.

Mathematical phantom generation. (a) Pre-contrast image with fiducial markers overlaid in red, (b) post-contrast image with fiducial markers overlaid in green, (c) Pre-contrast image with generated deformation field overlaid using color coding, (d) deformed image, (e) synthesized post-contrast image, (f) simulated contrast-enhancement.

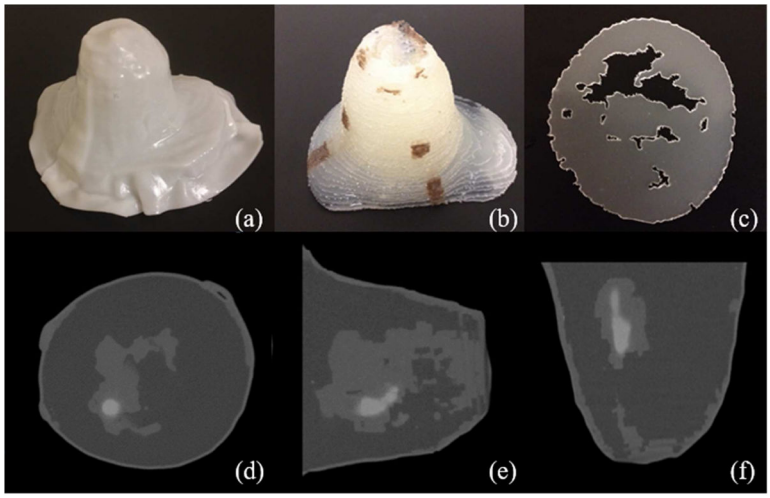

Figure 5.

The physically-deformable breast phantom. (a) Thermoplastic cast representing the skin, (b) polyethylene slabs representing the adipose tissue, (c) an individual polyethylene slab with glandular cavities, (d–f) coronal, sagittal and transvers views of the post-contrast phantom with the contrast-enhanced lesion shown.

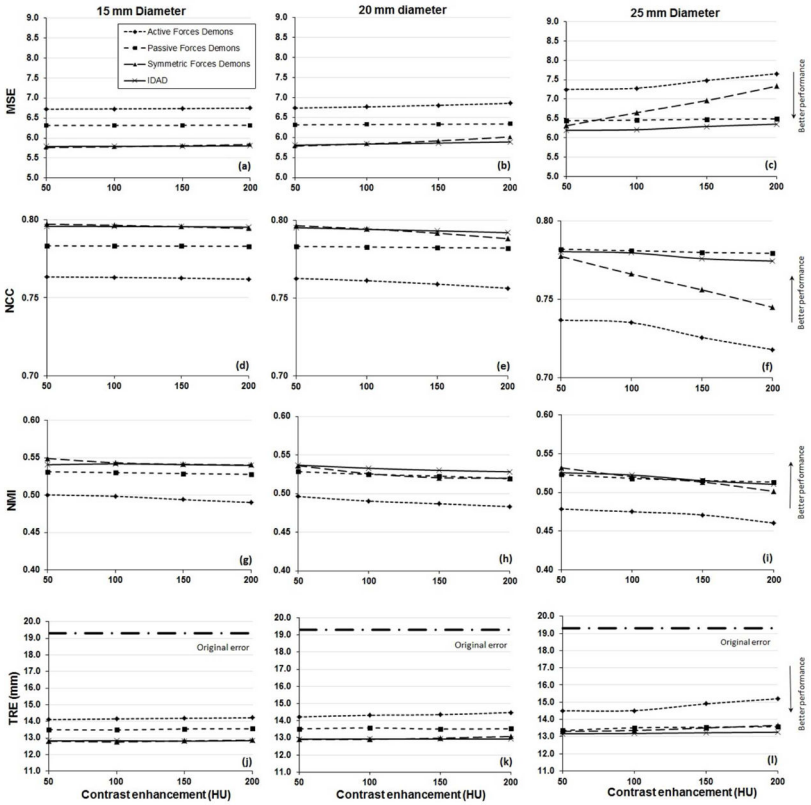

Figure 6.

Comparison between different variations of Demons for different levels and volumes of contrast enhancement: (a–c): MSE evaluation, (d–f): NCC evaluation, (g–i): NMI evaluation, (j–l): TRE evaluation. For MSE, NCC and NMI evaluations, the deformations resulting from different Demons variations were compared to the template deformation field. In TRE evaluations, the registration error was calculated for all the bCT image voxels. The "original error" shows the error between the pre-contrast image and the synthesized post-contrast image

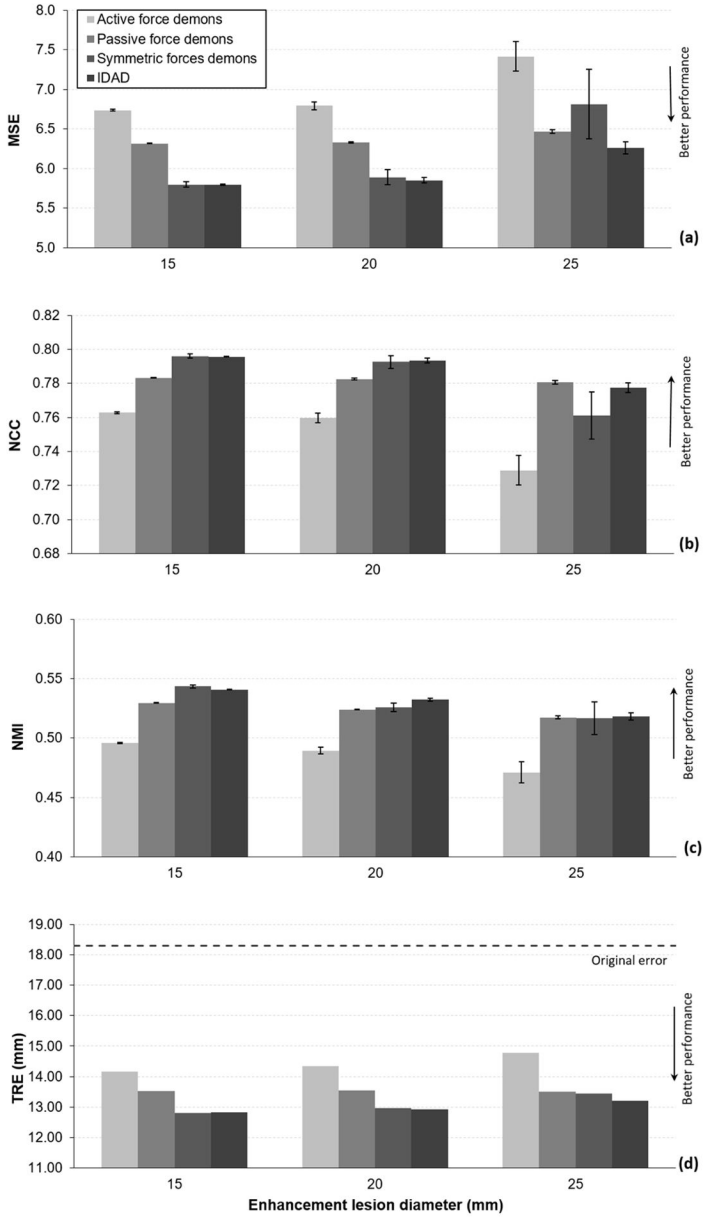

Figure 7.

Comparison between different variations of Demons at different volumes of contrast enhancement, (a) MSE, (b) NCC, (c) NMI and (d) TRE. The “original error” shows the error between the pre-contrast image and the synthesized post-contrast image. The error bars show the standard deviation over the employed enhancement levels.

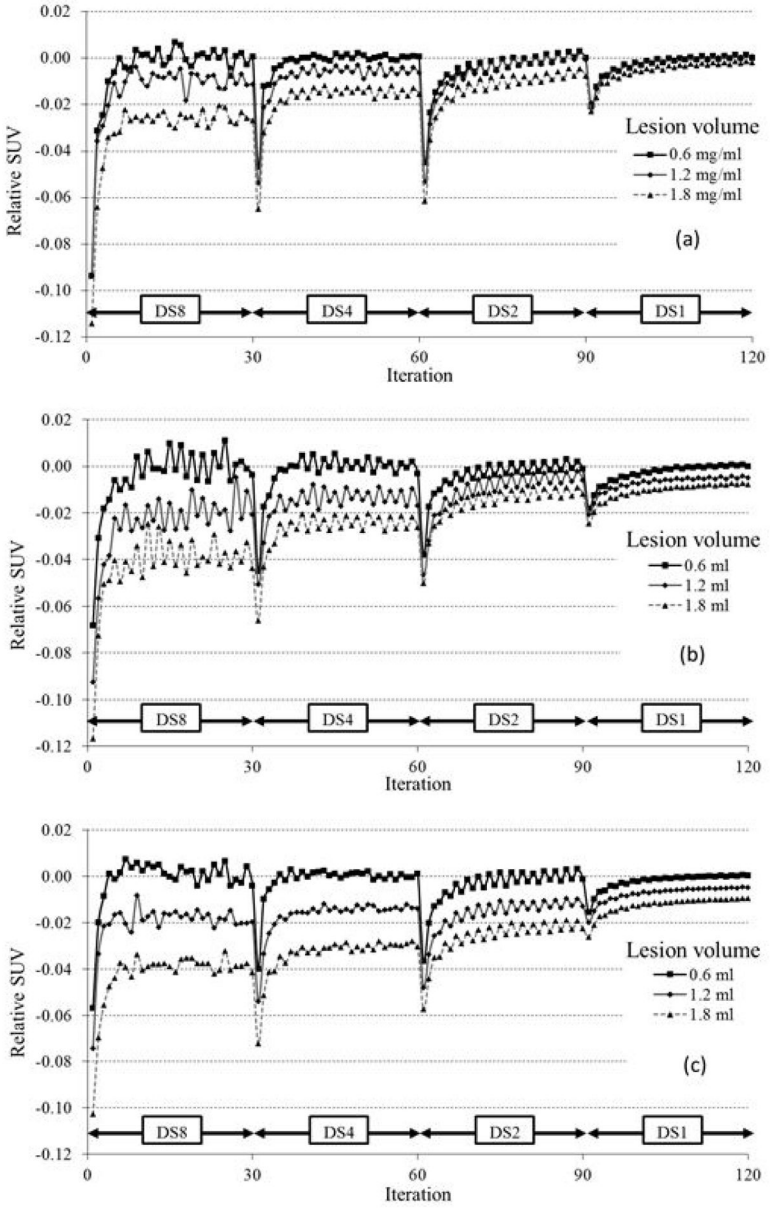

Figure 8.

Evolution of IDAD through the multiscale architecture with fixed number of iterations and different concentrations of contrast solution. (a) 1.62 mg/ml contrast solution, (b) 3.24 mg/ml contrast solution, (a) 4.86 mg/ml contrast solution.

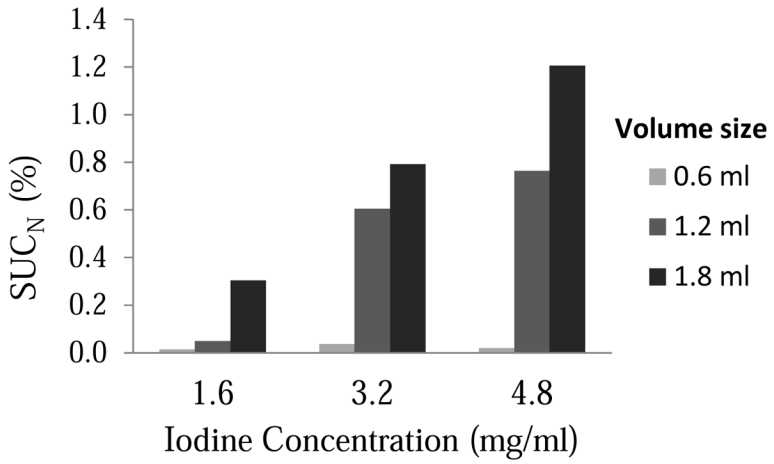

Figure 9.

Comparison between the final structural errors of the physical phantom registered images. Different volumes of the infused contrast-enhanced lesion within the deformable phantom are considered.

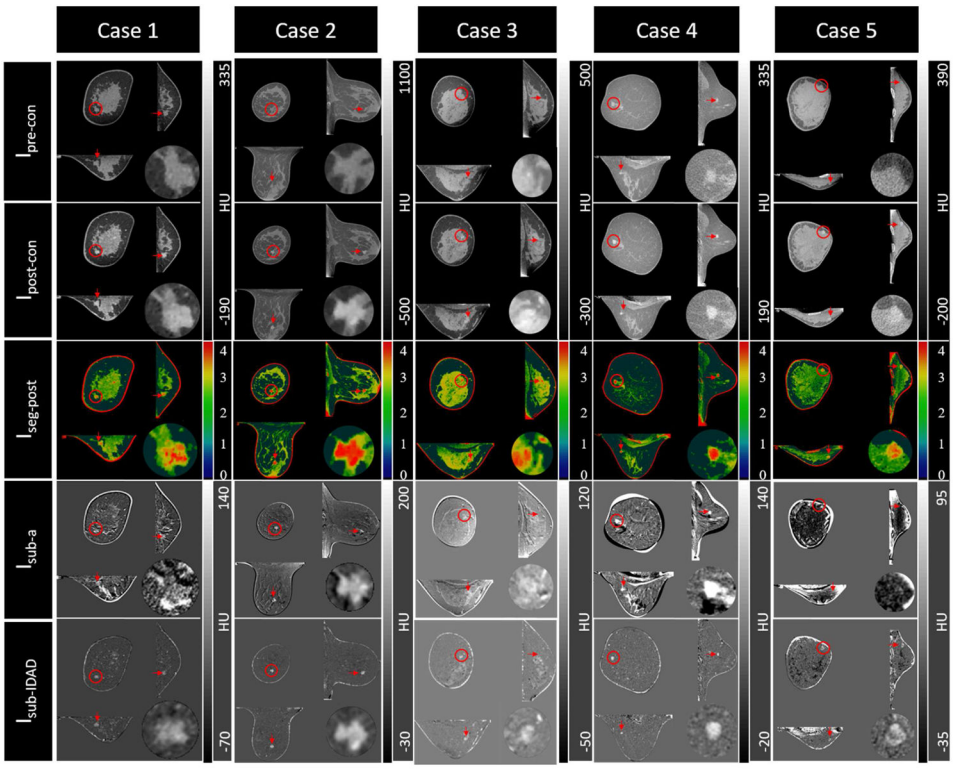

Figure 10.

Illustration of bCT datasets. In each image within a dataset, the anatomical views of the contrast-enhanced lesion are shown in coronal (upper left), sagittal (upper right), transverse (lower left) and magnified coronal (lower right) sub images. Each column represents a case. Rows show the results of different stages of IDAD: $I_{pre\text{-}con}$ (original pre-contrast image), $I_{post\text{-}con}$ (original post-contrast image), $I_{seg\text{-}post}$ (segmented post-contrast image), $I_{sub\text{-}a}$ (result of subtraction of post-affine registered pre-contrast image from post-contrast image), $I_{sub\text{-}IDAD}$ (result of subtraction of post-IDAD registered pre-contrast image from post-contrast image). The position of the contrast-enhanced lesion is shown in red in each sub image.

Table 1

Summary of notations

n_{LB}	Histogram bin index associated with histogram lower bound value
n_{MB}	Histogram bin index associated with histogram mid-bound value
n_{HB}	Histogram bin index associated with histogram higher bound value
H	Image histogram
N	Total number of histogram bins
n	Histogram bin index
HU_{max}	Maximum Hounsfield unit of image
HU_{min}	Minimum Hounsfield unit of image
AV_{HI}	Average value of histogram higher interval
AV_{LI}	Average value of histogram lower interval
ε	Two-means clustering method convergence threshold
T_1	Two-means clustering first threshold
T_2	Two-means clustering second threshold
P_{FG}	Histogram bin associated with histogram fibroglandular peak value
P_A	Histogram bin associated with histogram adipose peak value
P_c	Histogram bin associated with histogram contrast peak value
T_A	Histogram bin associated with adipose threshold
T_{FG}	Histogram bin associated with fibroglandular threshold
T_C	Histogram bin associated with contrast enhancement threshold
$D(p)$	Deformation vector at voxel p
I	An Image set to fixed or moving images
$I_{pre\text{-}con}$	Pre-contrast image
$I_{post\text{-}con}$	Post-contrast image
I_s	Smoothed image
I_a	Affine-registered pre-contrast image
I_{IDAD}	IDAD-registered pre-contrast image
$I_{seg\text{-}post}$	Post-contrast segmented image
I_{sub}	Subtraction result between $I_{post\text{-}con}$ and $I_{pre\text{-}con}$
$I_{sub\text{-}a}$	Subtraction result between $I_{post\text{-}con}$ and I_a
$I_{sub\text{-}IDAD}$	Subtraction result between $I_{post\text{-}con}$ and I_{IDAD}
M	Moving image
F	Fixed image
σ	Image intensity noise
k	normalization factor
Δ	Image gradient
c	Intensity Difference Correction Factor (IDCF)

DS8	Downsampled image (8×8×8 voxel binning)
DS4	Downsampled image (4×4×4 voxel binning)
DS2	Downsampled image (2×2×2 voxel binning)
DS1	Downsampled image (1×1×1 voxel binning)

Table 2

Summary of the materials used in development of deformable breast phantom

Material		**Average CT Number (HU)**
Adipose tissue surrogate	Polyethylene	−84
	Corn oil	−90
Fibroglandular tissue surrogate	Alginic acid solution	5
Skin tissue surrogate	Thermoplastic	−8
Contrast-enhanced tissue surrogate	1.62 mg/ml I-$CaCO_3$ solution	56
	3.24 mg/ml I-$CaCO_3$ solution	126
	4.86 mg/ml I-$CaCO_3$ solution	190

Table 3

Summary of patient cases studied for IDAD evaluation

		Case 1	Case 2	Case 3	Case 4	Case 5
breast size (cm)	Diameter	12.5	14	11.7	18.2	17.1
	Length	6.5	10.8	6.9	10.2	6.4
Volume glandularity (%)		30.8	32.1	31.3	26.6	51.8
Contrast delay (sec)		90	75	72	91	81
Lesion of interest diameter (mm)		4.5	11.6	10.5	7.8	8.9
Average lesion enhancement (HU)		65	130	85	87	46
NCC	Pre-registration	0.9836	0.9936	0.9904	0.9659	0.9528
	Affine	0.9912	0.9946	0.9917	0.9834	0.9749
	Symmetric Demons	0.9980	0.9979	0.9976	0.9965	0.9902
	IDAD	0.9991	0.9985	0.9982	0.9971	0.9916
NMI	Pre-registration	0.4352	0.5477	0.5289	0.4909	0.3128
	Affine	0.4907	0.5653	0.5498	0.6135	0.4154
	Symmetric Demons	0.6124	0.6498	0.6415	0.7714	0.5184
	IDAD	0.6360	0.6521	0.6592	0.7727	0.5250
MSE	Pre-registration	26196.0	9871.9	15034.4	47288.4	74064.4
	Affine	14131.2	8305.7	12977.2	25515.2	39921.2
	Symmetric Demons	1366.7	2386.2	2981.4	4102.1	13450.1
	IDAD	1335.1	2299.7	2722.3	4024.9	13168.7
Mean TRE (mm)	Pre-registration	3.2 ± 0.8	2.5 ± 0.8	2.7 ± 2.3	5.1 ± 3.8	9.1 ± 4.4
	Affine	2.2 ± 0.4	1.6 ± 0.4	1.8 ± 2.0	3.8 ± 2.0	5.3 ± 2.0
	Symmetric Demons	0.8± 0.5	0.8± 0.2	0.9± 0.6	0.7± 0.3	1.2± 1.1
	IDAD	0.8± 0.4	0.8± 0.4	0.8 ± 0.8	0.8 ± 0.4	1.2 ± 1.6